Compact radio emission indicates a structured jet was produced by a binary neutron star merger

Ghirlanda, G.; Salafia, O.S.; Paragi, Z.; Giroletti, M.; Yang, J.; Marcote, B.; ... ; Zhang, M.

Re-solving the jet/cocoon riddle of the first gravitational wave with an electromagnetic counterpart

[1,2,12]*G. Ghirlanda, [1,2,12]*O. S. Salafia, [3]Z. Paragi, [4]M. Giroletti, [5]J. Yang, [3]B. Marcote, [3]J. Blanchard, [6]I. Agudo, [22]T. An, [7]M. G. Bernardini, [8]R. Beswick, [9,26]M. Branchesi, [1]S. Campana, [10]C. Casadio, [11]E. Chassande–Mottin, [2,12]M. Colpi, [1]S. Covino, [1]P. D'Avanzo, [13]V. D'Elia, [14]S. Frey, [15]M. Gawronski, [1]G. Ghisellini, [3,16]L.I. Gurvits, [17,18]P.G. Jonker, [3,19]H. J. van Langevelde, [1]A. Melandri, [8]J. Moldon, [1]L. Nava, [12]A. Perego, [6]M. A. Perez-Torres,[20]C. Reynolds, [21]R. Salvaterra, [1]G. Tagliaferri, [4]T. Venturi, [23]S. D. Vergani, [24,25]M. Zhang

[1]Istituto Nazionale di Astrofisica - Osservatorio Astronomico di Brera, Via E. Bianchi 46, I-23807 Merate, Italy
[2]Dipartimento di Fisica G. Occhialini, Università di Milano-Bicocca, Piazza della Scienza 3, IT-20126 Milano, Italy
[3]Joint Institute for VLBI ERIC, Oude Hoogeveensedijk 4, 7991 PD Dwingeloo, The Netherlands
[4]Istituto Nazionale di Astrofisica - Istituto di radioastronomia, via Gobetti 101, I40129, Bologna, Italia
[5]Chalmers University of Technology, Onsala Space Observatory, SE-439 92, Sweden
[6]Instituto de Astrofísica de Andalucía-CSIC, Glorieta de la Astronomía s/n, E-18008, Granada, Spain
[7]Laboratoire Univers et Particules de Montpellier, Universitè de Montpellier, CNRS/IN2P3, place Eugéne Bataillon, F--34085 Montpellier, France
[8]e-MERLIN/VLBI National facility, Jodrell Bank Centre for Astrophysics, The School of Physics and Astronomy, The University of Manchester, United Kingdom
[9]Gran Sasso Science Institute, Viale F. Crispi 7, I-67100, L'Aquila, Italy
[10]Max Planck Institute fur Radioastronomie Auf dem Huegel 69, Bonn D-53121, Germany
[11]APC, AstroParticule et Cosmologie, Université Paris Diderot, CNRS/IN2P3, CEA/Irfu, Observatoire de Paris, Sorbonne Paris Cité, F-75205 Paris Cedex 13, France
[12]Istituto Nazionale Fisica Nucleare, Sezione di Milano Bicocca, Piazza della Scienza 3, 20126 Milano, Italy
[13]Space Science Data Center, ASI, Via del Politecnico, s.n.c., 00133, Roma, Italy
14Konkoly Observatory, MTA Research Centre for Astronomy and Earth Sciences, Konkoly Thege Miklòsùt 15-17, H-1121 Budapest, Hungary
[15]Centre for Astronomy, Faculty of Physics, Astronomy and Informatics,Nicolaus Copernicus University, Grudziadzka 5, 87-100 Torun, Poland
[16]Department of Astrodynamics and Space Missions, Delft University of Technology, Kluyverweg 1, 2629 HS Delft, The Netherlands
[17]SRON, Netherlands Institute for Space Research, Sorbonnelaan 2, 3584 CA Utrecht, The Netherlands
[18]Department of Astrophysics/IMAPP, Radboud University, P.O. Box 9010, 6500 GL Nijmegen, the Netherlands
[19]Sterrewacht Leiden, Leiden University, P.O. Box 9513, NL-2300 RA Leiden, The Netherlands
[20]CSIRO Astronomy and Space Science, PO Box 1130, Bentley WA 6102, AU
[21]Istituto Nazionale di Astrofisica, IASF, via E. Bassini 15, 20133 Milano, IT

[22] Shanghai Astronomical Observatory, Key Laboratory of Radio Astronomy, Chinese Academy of Sciences, 200030 Shanghai, China
[23]GEPI Observatoire de Paris, CNRS UMR 8111, Meudon, FR
[24]Xinjiang Astronomical Observatory, Chinese Academy of Sciences, 150 Science 1-Street, Urumqi 831001, China
[25]Key Laboratory for Radio Astronomy, Chinese Academy of Sciences, 2 West Beijing Road, Nanjing 210008, China
[26]INFN - Laboratori Nazionali del Gran Sasso, I-67100 L'Aquila, Italy

*To whom correspondence should be addressed; E-mail: giancarlo.ghirlanda@brera.inaf.it, omsharan.salafia@brera.inaf.it

The first binary neutron star merger, detected through both electromagnetic radiation and gravitational waves on the 17th of August 2017, raised the question whether a narrow relativistic jet or a more isotropic outflow was launched as a consequence of the merger. High resolution measurements of the source size and position can provide the answer. Very Long Baseline Interferometry observations, performed 207.4 days after the binary merger through a global network of 32 radio telescopes spread over five continents, constrain the apparent source size to be smaller than 2 milliarcseconds at the 90% confidence level. This excludes the possibility that a nearly isotropic, mildly relativistic outflow is responsible for the emission, as in this case its apparent size, after more than six months of expansion, should have been significantly larger and resolved by the VLBI observation. Our size measurement proves that in at least 10% of neutron star mergers a structured relativistic jet should be produced.

One Sentence Summary: Size measurement through worldwide radio telescope array proves that relativistic jet successfully emerged from neutron star merger GW170817

GW170817 encodes two breakthrough discoveries: the detection of gravitational waves (GW) produced by the inspiral of two neutron stars (*1*) and the discovery of electromagnetic (EM) emission shortly following the merger (*2*). The history of this astrophysical transient, still unique in its class, is marked by a series of milestones. Less than two seconds after the detection of the GW event by the LIGO and Virgo interferometers, a weak short duration γ-ray burst (GRB 170817A) hit the space-based detectors (*3, 4*). Eleven hours later, electromagnetic emission was detected in ultraviolet to near-infrared wavelengths (*2*), pinpointing the host galaxy NGC 4993 at ~ 41 Mpc distance. The temporal and spectral properties of this emission component reflect those expected for a "kilonova", i.e. the radioactive-decay-powered emission from material ejected during and after the neutron star merger (*5, 6*). Finally, respectively 9 and 16 days after the GW event, X-ray (*7, 8*) and radio (*9*) emissions were detected. These are currently interpreted as being the afterglow of GRB 170817A. Monitoring of the afterglow emission with the largest radio (Karl Jansky Very Large Array – JVLA, Australian Telescope Compact Array – ATCA and Giant Metrewave Radio Telescope – GMRT), optical (Hubble Space Telescope – HST, Large Binocular Telescope – LBT) and X-ray (XMM-Newton and Chandra X-ray Observatory)

telescopes showed an unexpected slow achromatic flux–rise (*10*) ($F \propto t^{0.8}$) until ~ 150 days (*11–13*). Past this epoch, the source entered a decaying phase (*14, 15*).

Among the scenarios that are compatible with the radio, optical and X-ray long lived emission, the two most favored invoke the launch of a jet by the remnant of the merger. The jet drills a hole in the kilonova material ejected shortly before. Either the jet successfully breaks out of the ejecta, developing an angular structure (i.e. the energy and Lorentz factor scale with the angular distance from the jet axis – see Supplementary Text), or it fails to break out of the merger ejecta, depositing all its energy into the ejecta and forming a hot cocoon which subsequently expands due to its high pressure (*16–19*). In the latter case the energy is expected to be distributed over a significantly wider opening angle, and the expansion velocity is expected to be only mildly relativistic. Owing to the angular structure, the successful jet is often called "structured jet" (*20, 21*) while the choked jet cocoon is sometimes referred to only as the "choked jet" or as the "cocoon".

The present light curve of GRB 170817A (Figure 3), including the most recent (up to ~230 days) optical and radio observations (*15, 22*), cannot disentangle conclusively the two scenarios: with reasonable parameters, both models are consistent with all current observations (Figure 3). Independent probes are thus necessary. The geometry of the relativistic outflow can be tested through polarization measurements and/or imaging (*23–25*). Due to its higher velocity and narrower opening angle, the structured jet should show a larger displacement from the explosion origin and it should still (at ~200 d) appear compact, with an angular size smaller than 2 milliarcseconds (mas) (*23, 25*). The choked jet cocoon is expected to produce a smaller displacement (virtually no displacement and a ring image for a perfectly isotropic outflow) and a larger apparent angular size (larger than about 3 mas - Figure 2). The recent measurement of the displacement of the source apparent position by 2.67 ± 0.3 mas in 155 days (*22*) strongly supports the structured jet scenario. However, those data do not have sufficient resolution to place stringent limits on the size. Our global VLBI observations have the capability to place tighter limits on the source angular size, giving an independent constraint on the outflow geometry and its degree of collimation.

Results. We have observed GRB 170817A on March 2018 12-13, 207.4 days after the GW/GRB detection, under the global VLBI project (GG084) which involved 32 radio telescopes in 5 continents. The longest baseline producing useful data was 11878 km between Hertebeesthoek (South Africa) and Fort Davis (USA). Observations were performed at a central frequency of 4.85 GHz with a total bandwidth of 256 MHz. The total on-source time was 7.8 hours (see Materials and Methods).

We have detected a source at the sky position RA = $13^h09^m48.0688006 \pm 0.000014^s$, DEC = $-23^\circ22'53.390765 \pm 0.000245''$ (1σ statistical uncertainty – see Materials and Methods). This is compatible with the position of the source obtained with the High Sensitivity Array (HSA) (*22*) and within the uncertainty region of the astrometrically corrected HST source (*9*). With respect to the first HSA observation (*22*), at 75 days after the GW event, our position, measured at 207.4 days, is displaced by δRA(207.4 d − 75 d) = 2.44 ± 0.24 mas and δDEC(207.4 d − 75 d) = 0.14 ± 0.47 mas. With respect to the second epoch HSA observation (230 days), we measure δRA(230 d − 207.4 d) = 0.46 ± 0.27 mas and δDEC(230 d − 207.4 d) = 0.07 ± 0.47 mas (1σ statistical errors). The Global VLBI observation, performed shortly after the source flux density peak, is intermediate between the two HSA observations (inset in the upper left panel of Figure 1) and confirms the evidence of apparent superluminal motion reported by (*22*). From the global VLBI

image we measure a flux density of 42 ± 8 μJy at 5 GHz. This flux density is consistent with the value 47 ± 9 μJy obtained by interpolating the closest JVLA detections (*11, 15*) and also with the flux density upper limit (60 μJy at 3σ significance) obtained through our simultaneous observations with the e-MERLIN (see Materials and Methods). The image (Figure 1 - top left panel) shows a compact source, apparently unresolved on the scales of our synthetic beam of 1.5 × 3.5 mas (see Materials and Methods). We estimate (see Materials and Methods) that the source size at 207 days as measured from the global VLBI image is smaller than 2.0 mas at the 90% confidence level (Figure S3).

Discussion. We compared the source image with four possible models of the outflow, consisting of a successful jet and three choked jet models. The successful jet model parameters are determined by the simultaneous fit of the 3 GHz, optical and X-ray light curves and of the observed centroid displacement (obtained by comparing our position to those of (*22*)). The three choked jet models are characterized by different degrees of anisotropy, parametrized by the outflow collimation angle θ_c ranging from 30 to 60 degrees, all seen under a 30 degrees viewing angle. All three choked jet models fit the observed multi-wavelength light curves well. In all four cases, model images (Figure 2) are convolved to the primary beam of our global VLBI observation and a noise map of the field is added. The resulting synthetic maps for the successful jet and the 30 and 45 degrees cocoons are shown in Figure 1 (upper right panel and bottom panels). For the synthetic structured jet model image (Figure 1 top right panel), the measured flux density is consistent with the observed one, and the source appears unresolved with a size smaller than 2 mas.

The choked jet cocoon models with opening angles of 45 and 60 degrees (only the 45 degrees cocoon model is shown in the bottom panel of Figure 1), which would produce sources sizes > 3 mas (Figure 2), are excluded by our observations (see Materials and Methods). In these cases, with our beam, we should have measured a flux density significantly smaller than 42 ± 9 μJy, which would probably have resulted in a non-detection. The choked jet model with an opening angle of 30 degrees produces an image (bottom left panel of Figure 1) whose size is marginally consistent with our limit, and whose peak flux density is marginally consistent with our measurement. On the other hand, no choked jet model is able to reproduce the very fast observed centroid motion (*22*), confirmed by our intermediate-epoch global VLBI observation. The best explanation for the multi-wavelength observations of GRB 170817A is thus a successful jet endowed with an angular velocity and energy profile, featuring a narrow ($\theta_c = 3.4 \pm 1°$) and energetic ($E_{iso,core} = 2.5^{+7.5}_{-2.0} \times 10^{52}$ erg) core seen under a viewing angle of ~15 degrees. Its synthetic image (top right panel of Figure 1) is remarkably similar to the source image (top left panel of Figure 1). The energy and bulk velocity of the jet material decrease steeply away from the jet axis (see Supplementary Text) – we call "sheath" this slower material surrounding the core. The low luminosity ($L_{iso} \sim 10^{47}$ erg s^{-1}) of the short GRB170817, detected by the Fermi satellite 1.7 s after the GW event (*3*), was most likely not produced by the jet core (whose emission was too relativistically beamed to intercept our line of sight), but rather by the part of the sheath moving in our direction; the multi-wavelength slowly rising emission (*10, 11, 13*) was due to the subsequent deceleration of parts of the sheath progressively closer to the core. The flattening (*13*) and subsequent peak (*15*) of the light curve (Figure 3) mark the time after which the emission is dominated by the jet core.

If such a jet were observed on-axis, its gamma-ray emission would have had an isotropic equivalent luminosity $\geq 10^{51}$ erg s^{-1} (assuming 10% efficiency in the conversion of kinetic energy to radiation). The most recent studies of sGRB luminosity function (*26, 27*) agree that the local rate of sGRB with $L_{iso} > 10^{51}$ erg s^{-1} is ~ 0.5 yr^{-1} Gpc^{-3}. Assuming that all sGRB jets have a similar (i.e. quasi-universal (*28*)) structure, and that sGRB with $L_{iso} > 10^{51}$ erg s^{-1} are produced by jets whose core points towards the Earth, the rate of lower luminosity events increases according to the jet structure (*29*) due to the progressively larger number of events observed under larger viewing angleθ_v. For a structured jet whose luminosity scales as a power-law (*28*) $L(\theta_v) \propto (\theta_v/\theta_c)^{-\alpha}$, the local rate $R_0(>L)$ of events with luminosity larger than L is shown in Figure 4 for $\alpha = 2, 3, 4$. Based on the Fermi detection (*30*), the rate of GRBs with luminosity as low as GRB 170817A (Figure 4) is consistent with the luminosity function of structured jets. Comparing the resulting rate of jets to the local rate of NS–NS mergers, $R_{NS-NS} = 1540^{+3200}_{-1220}$ yr^{-1} Gpc^{-3} as estimated by the LIGO and Virgo Collaborations (*1*), we argue that at least 10% of NS-NS mergers launch a jet which successfully breaks out of the merger ejecta.

References and Notes:

1. B. P. Abbott, *et al.*, *Physical Review Letters* 119, 161101 (2017).
2. D. A. Coulter, *et al.*, *Science* p. eaap9811 (2017).
3. A. Goldstein, *et al.*, *The Astrophysical Journal* 848, L14 (2017).
4. V. Savchenko, *et al.*, *The Astrophysical Journal* 848, L15 (2017).
5. E. Pian, *et al.*, *Nature* 551, 67 (2017).
6. S. J. Smartt, *et al.*, *Nature* (2017).
7. E. Troja, *et al.*, *Nature* (2017).
8. R. Margutti, *et al.*, *The Astrophysical Journal* 848, L20 (2017).
9. G. Hallinan, *et al.*, *Science* p. eaap9855 (2017).
10. K. P. Mooley, *et al.*, *Nature* (2017).
11. R. Margutti, *et al.*, *The Astrophysical Journal* 856, L18 (2018).
12. E. Troja, *et al.*, *Monthly Notices of the Royal Astronomical Society: Letters* (2018).
13. P. D'Avanzo, *et al.*, *Astronomy & Astrophysics* (2018).
14. D. Dobie, *et al.*, *ArXiv e-prints* (2018).
15. K. D. Alexander, *et al.*, *ArXiv e-prints* (2018).
16. E. Ramirez-Ruiz, A. Celotti, M. J. Rees, *MNRAS* 337, 1349 (2002).
17. E. Nakar, T. Piran, *MNRAS* 478, 407 (2018).
18. D. Lazzati, *et al.*, *ApJL* 848, L6 (2017).
19. O. Gottlieb, E. Nakar, T. Piran, *MNRAS* 473, 576 (2018).
20. E. Rossi, D. Lazzati, M. J. Rees, *MNRAS* 332, 945 (2002).
21. B. Zhang, P. Me´sza´ros, *ApJ* 571, 876 (2002).
22. K. P. Mooley, *et al.*, *ArXiv e-prints* (2018).
23. R. Gill, J. Granot, *MNRAS* (2018).
24. J. Granot, F. De Colle, E. Ramirez-Ruiz, *ArXiv e-prints* (2018).
25. J. Zrake, X. Xie, A. MacFadyen, *ArXiv e-prints* (2018).
26. G. Ghirlanda, *et al.*, *A&A* 594, A84 (2016).
27. D. Wanderman, T. Piran, *MNRAS* 448, 3026 (2015).
28. O. S. Salafia, G. Ghisellini, A. Pescalli, G. Ghirlanda, F. Nappo, *MNRAS* 450, 3549 (2015).
29. A. Pescalli, *et al.*, *MNRAS* 447, 1911 (2015).

30. B.-B. Zhang, *et al.*, *Nature Communications* 9, 447 (2018).
31. L. Resmi, *et al.*, *ArXiv e-prints* (2018).
32. A. Keimpema, *et al.*, *Experimental Astronomy* 39, 259 (2015).
33. Z. Paragi, *et al.*, *GCN Circulars* 21763, 1 (2017).
34. Z. Paragi, *et al.*, *GCN Circulars* 21939, 1 (2017).
35. E.W.Greisen, *Information Handling in Astronomy-Historical Vistas*, A.Heck, ed.(2003), vol. 285 of *Astrophysics and Space Science Library*, p. 109.
36. C. Reynolds, Z. Paragi, M. Garrett, *ArXiv Astrophysics e-prints* (2002).
37. M. C. Shepherd, *Astronomical Data Analysis Software and Systems VI*, G. Hunt, H. Payne, eds. (1997), vol. 125 of *Astronomical Society of the Pacific Conference Series*, p. 77.
38. I. Andreoni, *et al.*, *PASA* 34, e069 (2017).
39. D. Foreman-Mackey, D. W. Hogg, D. Lang, J. Goodman, *PASP* 125, 306 (2013).
40. The LIGO Scientific Collaboration, *et al.*, *ArXiv e-prints* (2018).
41. P. Kumar, J. Granot, *Astrophys. J.* 591, 1075 (2003).
42. D. Lazzati, *et al.*, *arXiv e-prints* (2017). 10
43. J. D. Lyman, *et al.*, *arXiv e-prints* (2018).
44. A. Panaitescu, P. Kumar, *The Astrophysical Journal* 543, 66 (2000).
45. K. Hotokezaka, *et al.*, *The Astrophysical Journal* 831, 190 (2016).
46. R. D. Blandford, C. F. McKee, *Physics of Fluids* 19, 1130 (1976).

Acknowledgments: We wish to acknowledge M. E. Ravasio, I. Andreoni and A. Deller for help in cross-checking the AGN position. The European VLBI Network is a joint facility of independent European, African, Asian, and North American radio astronomy institutes. Scientific results from data presented in this publication are derived from the EVN project codes GG084 (PI G. Ghirlanda), RG009 (PI G. Ghirlanda), EP105 (PI Z. Paragi) and from the e-MERLIN project code CY6213 (PI G. Ghirlanda).

Funding: The National Institute of Astrophysics is is acknowledged for PRIN-grant (2017) 1.05.01.88.06. The Italian Ministry for University and Research (MIUR) is acknowledged through the project "FIGARO" (Prin-MIUR) grant 1.05.06.13. The research leading to these results has received funding from the European Commission Horizon 2020 Research and Innovation Programme under grant agreement No. 730562 (RadioNet). The Spanish Ministerio de Economa y Competitividad (MINECO) is acknowledged for financial support under grants AYA2016-76012-C3-1-P, FPA2015-69210-C6-2-R, and MDM-2014-0369 of ICCUB (Unidad de Excelencia "Mara de Maeztu"). ECM and BC acknowledge support from the European Unions Horizon 2020 research and innovation programme under grant agreement No.653477. SF thanks the Hungarian National Research, Development and Innovation Office (OTKA NN110333) for support. The Long Baseline Array is part of the Australia Telescope National Facility which is funded by the Australian Government for operation as a National Facility managed by CSIRO. e-MERLIN is a National Facility operated by the University of Manchester at Jodrell Bank Observatory on behalf of STFC. This publication has received funding from the European Union's Horizon 2020 research and innovation programme under grant agreement No. 730562 [RadioNet].

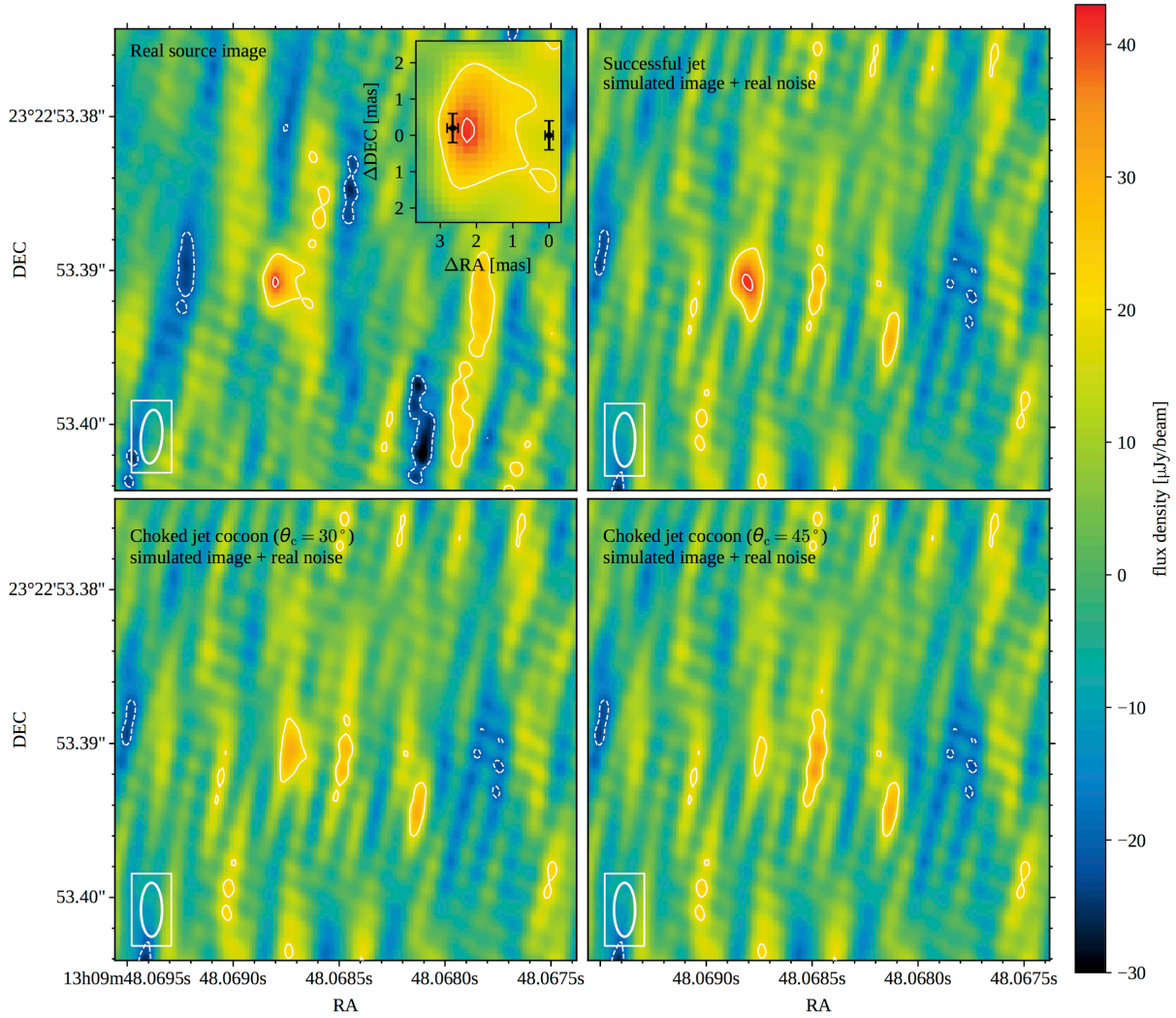

Fig. 1. Real and simulated radio images. Top left panel: radio image from our global-VLBI observation (measured rms of 8 μJy). Inset: zoom on the source, with black error bars showing previously reported (*22*) centroid positions at 75 days and 230 days. The tick marks on the axes show the projected distance in milliarcseconds from the position at 75 days. Top right panel: simulated successful jet radio image with real noise added. Bottom left panel: simulated choked jet cocoon (with $\theta_c = 30^\circ$) radio image with real noise added. Bottom right panel: simulated choked jet cocoon (with $\theta_c = 45^\circ$) radio image with real noise added. The white contours correspond to flux densities -20, 20 and 40 μJy. The beam size (3.5x1.5 mas) is shown on the bottom left of each panel.

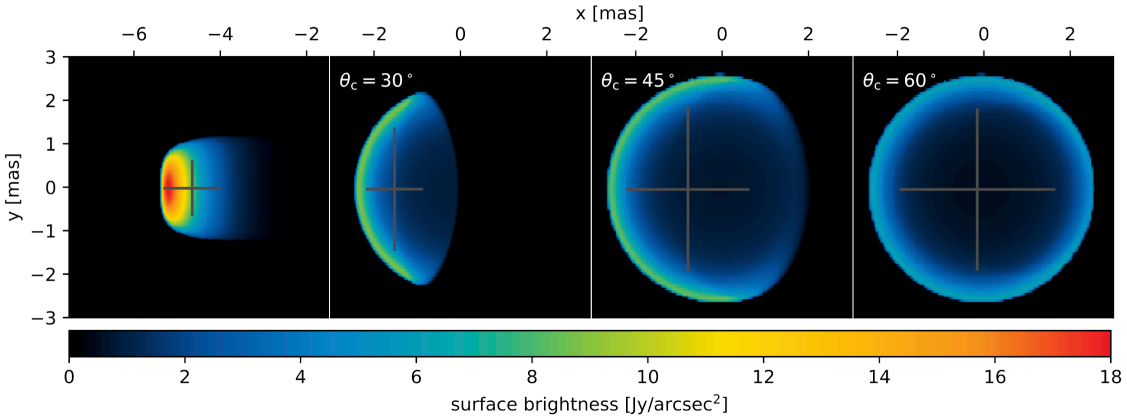

Fig. 2. Model images. Leftmost panel: predicted structured jet radio surface brightness distribution. Remaining panels: predicted choked jet cocoon radio surface brightness distributions for three different effective opening angles, namely $\theta_c = 30^\circ, 45^\circ, 60^\circ$, as shown on the figures. The grey crosses, centered at the image centroid, show a measure of the equivalent full width half maximum of the surface brightness distributions along the axes. In each figure, the origin of the coordinates marks the projected position of the progenitor neutron star binary merger.

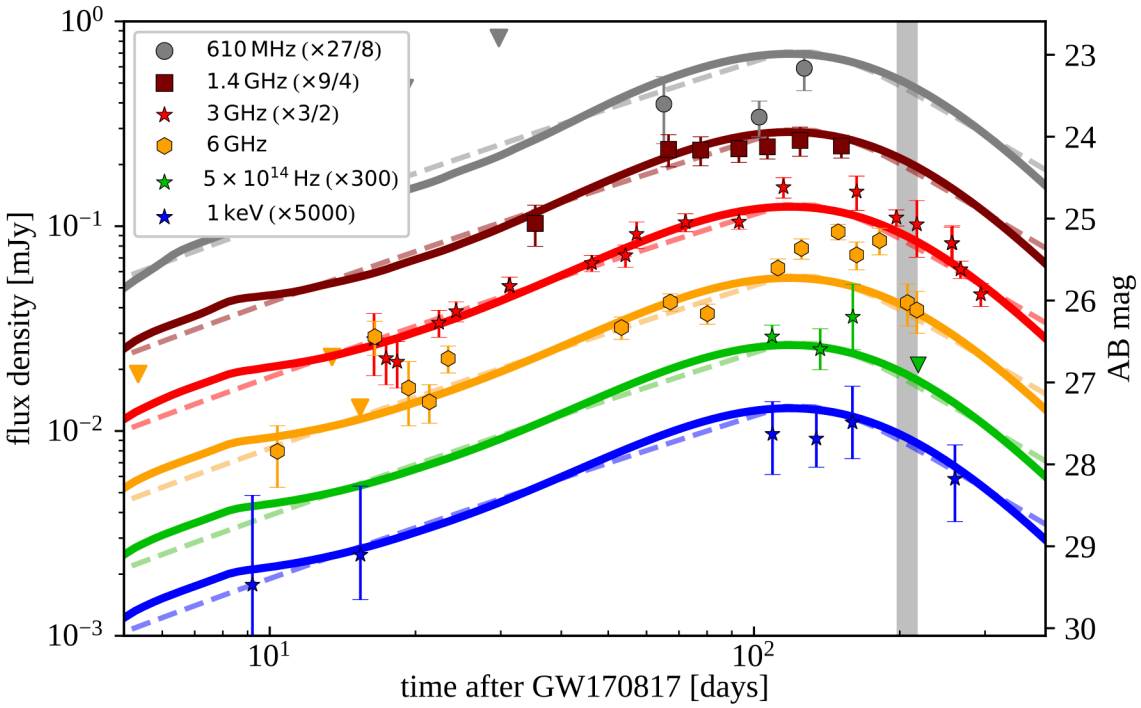

Fig. 3. Multiwavelength light curve. Up to date multi-wavelength light curve of the target source GRB 170817A. Model curves are for structured jet model (solid lines) and isotropic outflow with velocity profile (dashed lines). Models are parametrised as described in Materials and Methods. Upper limits are shown by downward triangles. The data set reported in *(13)* has been updated with the latest published observations (*14,15,31*). The shaded grey vertical line marks the date of our global VLBI observation (project GG084). Data and model curves are shifted by multiplicative factors (shown in parenthesis in the legend) for the ease of display.

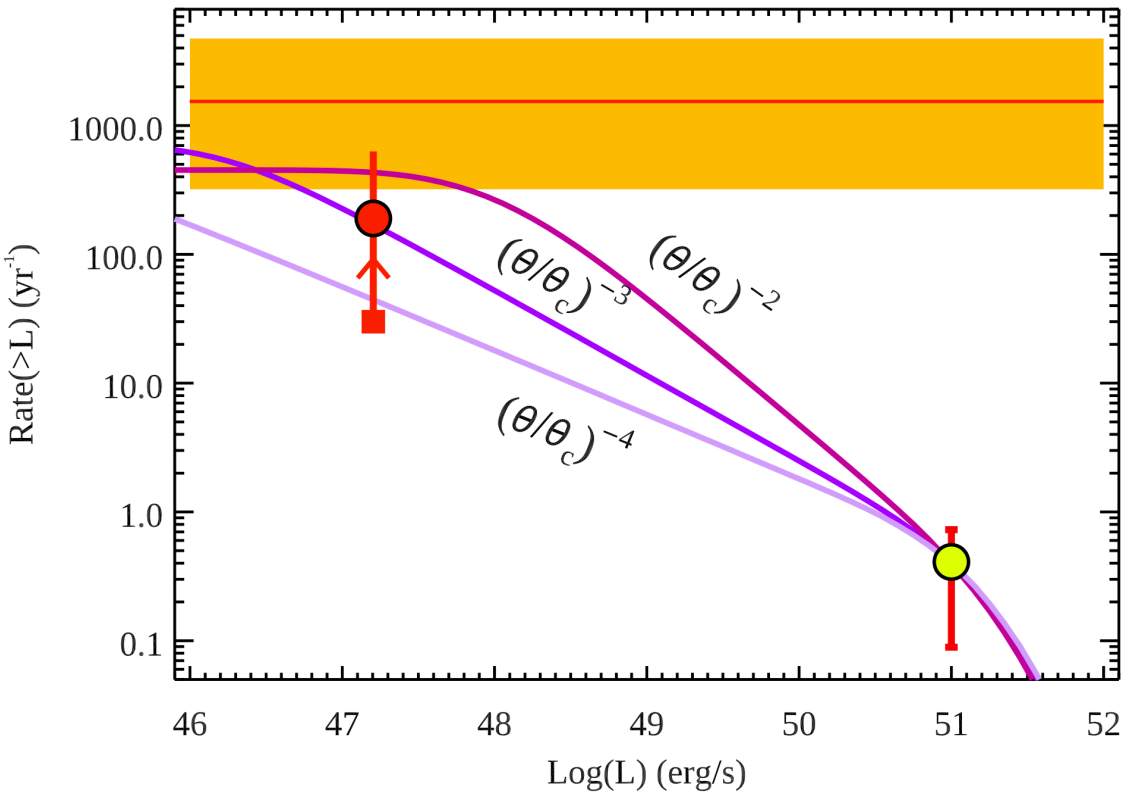

Fig. 4. Short GRB rate. The rate of short GRBs with isotropic equivalent luminosity Liso > 10^{51} erg s^{-1} (yellow filled symbol) compared with the expected rate of short GRBs similar to GRB 170817A (solid red symbol - (*30*) - this can be considered a lower limit as similarly dim sGRB detected by Fermi could have the same origin). Different jet structures, as labeled, predict a rate consistent with the estimate based on the detection of GRB 170817A by Fermi. The red solid horizontal line (shaded region is 1σ uncertainty) shows the rate of BNS mergers as inferred (*1*) by the GW170817 detection by LIGO/Virgo.

Materials and Methods

Global VLBI observations, data reduction and analysis.

The observations were carried out on March 2018 12–13 at 5 GHz with a global array of radio telescopes including ATCA (phased array of 5x22 m), Mopra, Ceduna and Hobart from the Long Baseline Array (LBA); Tianma, Urumqi, Badary, Kunming, Hartebeesthoek, Zelenchukskaya, Noto, Medicina, Effelsberg, Jodrell Bank MkII, Irbene 16m, Onsala 25m, Yebes, Torun, and Westerbork (single dish) from the European VLBI Network (EVN); eight telescopes from the Very Long Baseline Array (VLBA: Hancock, North Liberty, Fort Davis, Los Alamos, Kitt Peak, OVRO, Brewster, and Mauna Kea) and the R.C. Byrd Green Bank Telescope. Unfortunately the Karl Jansky Very Large Array (JVLA) did not take part because of a power failure. Westerbork, Torun, ATCA, Mopra and Ceduna recorded at a total bit rate of 1 Gbit/s, the rest of the array did 2 Gbit/s recording. Hobart had no fringes, and Ceduna sensitivity was very low. In addition, the sensitivity for all the EVN telescopes recording at 2 Gbit/s were lower than expected for certain subbands in this observing session of 2018, due to issues with the calibration control in the digital baseband converters (DBBC). The data were correlated at the Joint Institute for VLBI ERIC (JIVE) in Dwingeloo, the Netherlands, with the EVN Software Correlator (SFXC; (*32*)). The Irbene 16m data disk did not arrive in time for rapid correlation. The total recorded bandwidth was 256 MHz per polarization; most telescopes observed both left- and right-hand circular polarizations (Ceduna had right circular polarization only, Mopra had linear polarizations). This was divided into 16 × 16 MHz sub-bands during correlation. The correlator integration time was 1s and the spectral resolution was 0.5 MHz. The resulting field of view for an array extending to 12000 km was 8.25 arcseconds in radius (10% loss in amplitude), limited by bandwidth smearing. This means that the NGC 4993 AGN in the field of view of GRB 170817A was somewhat smeared for the longest baselines in our data.

Due to the very low declination – and thus very low elevations for telescopes in the northern hemisphere – the phase-referencing observations were quite challenging. We thus used a short phase-referencing cycle of 1.5 minutes on calibrator and 2.5 minutes on the target (both include slewing times). The phase-reference source was J1311−2329, separated by just 26 arcmin from both the target and the phase-referencing check source J1312−2350. The J2000 correlation position of J1311−2329 (RA = $13^{h}11^{m}37.413987^{s}$, DEC = −23°29′56.64651″) was determined by earlier EuroVLBI team observations on 11 October 2017 (project EP105A), with respect to the bright International Celestial Reference Frame (ICRF) source J1303−2405, which was used to calibrate all the early GRB 170817A observations by the group (*33, 34*). While our initial position on the phase-reference calibrator was accurate to about a few milliarcseconds, using the very nearby check source J1312−2350 allowed us to determine precise positions in the ICRF. In addition to the above mentioned sources, we used J1337−1257 as fringe-finder.

The data were reduced using the AIPS (*35*) package. As a first step, we followed the EVN Data Reduction Guide (http://www.evlbi.org/user guide/evn datareduc/index.html). We downloaded the IDI FITS files and the pipeline (*36*) calibration tables from the EVN data repository, and read them into AIPS. We copied over the second version of the pipeline calibration table (CL.2), the flag as well as the bandpass tables (FG.1, BP.1) to the data. In CL.2 parallactic angle correction and a-priori amplitude calibration information (using the Tsys and gains measured at the telescopes) are included. We ran TECOR to correct for the signal propagation delays caused by the ionosphere, using ionex files provided by the Jet Propulsion Laboratory (JPL) for the days of the observations. The instrumental delay and phase offsets between the different sub-bands were removed using 4 short scans of the calibrator sources (to

correct for the different parts of the array) with FRING. In the final fringe-fitting in order to determine the residual delays, rates and phases, we combined all the sub-bands to increase signal-to-noise ratio. For the GRB 170817A field and for the J1312−2350 check source we interpolated solutions from the reference source J1311−2329 using CLCAL. The calibration was applied to all sources and the frequencies within the sub-bands were averaged with SPLIT. To obtain the frequency-averaged data for NGC 4993, we shifted the GRB 170817A field phase-centre to the AGN position by UVFIX before SPLIT. Imaging and model-fitting were carried out by DIFMAP (*37*); we read the resulting images back to AIPS to fit it with JMFIT.

We detected GRB 170817A, the AGN in NGC 4993, and the phase-reference check source J1312−2350. The J1312−2350 data showed that phase-referencing in principle worked very well, with coherence losses not exceeding the 10–15% typically seen in VLBI under good atmospheric conditions. Our a-priori reference position of J1311−2329 was however erroneous for about 1.5 milliarcseconds, as is apparent by the comparison of our obtained positions with published ones (for GRB 170817A by (*22*), for NGC 4993 by (*38*), and for J1312−2350 compared to the known ICRF position). After re-referencing our GRB 170817A position to the known position of J1313−2350, we get RA = 13h09m48.0688006 ± 0.000014s, DEC = −23◦22′53.390765 ± 0.000245″, where the quoted errors are purely statistical reported by JMFIT. The source GRB 170817A is clearly the brightest in a field of view of 1×1 arcseconds in our naturally weighted dirty map and by applying a Gaussian-taper to the uv-data. The position IS within the 1-sigma error box reported earlier by the HST, and within 0.5 milliarcseconds of the position reported by (*22*) for April 2018.

e-MERLIN coordinated observations: data analysis and results.

Twelve coordinated observations with the e-MERLIN array were made between 8 and 22 March 2018 (project CY6213) in support of the global VLBI observations presented here. All data were correlated in real-time with a total bandwidth of 512 MHz covering the range 5 to 5.5 GHz, divided into four spectral windows each with 512 channels per polarisation. The observing band for these observations overlapped those used by VLBI. Given the low declination of the target and hence very low elevations for telescopes in e-MERLIN the available on-source observing time per observation was limited to ~5 hours and phase-referencing and on-sky amplitude calibration of these data was challenging. To mitigate this we used a short phase referencing cycle time (2:5.5min) between the target and phase-reference source J1311−2329, located at a distance of 0.43 deg from the target. Additionally periodic observations every 30 min were also made of the nearby ICRF source J1259−2310 . Standard data analysis procedures were undertaken using the NRAO CASA packages and utilizing the e-MERLIN data pipeline (http://www.emerlin.ac.uk/data red/). Images of the individual runs provide a noise level between 55 and 90 μJy/beam and a synthesized beam size of about 180×40 mas. A combined image of all the runs yield a 3-sigma upper limit on the source flux density of 60 μJy. When considering only the closest days to the EVN observation, from March 11 to 14, the upper limit is 100 μJy. The nucleus of the host galaxy NGC 4993 is detected on individual epochs with an average flux density and statistical uncertainty of 270 ± 50 μJy. The flux density of NGC 4993 from the combined dataset is 220 ± 20 μJy.

Estimation of the source size.

Our SNR is limited to around 5, thus determining the size of the radio emitting region is not straightforward. Fitting the map in AIPS by JMFIT does not give a conclusive answer whether

the source is resolved or not. Fitting a circular-Gaussian component in DIFMAP results a size of 2.9 mas, which is comparable to our naturally weighted (but untapered) beam size of 3.5 × 1.5 mas, with major axis position angle of −6 degrees. However, we consider this as an upper limit because the fitting procedure clearly overestimates the source flux (93 μJy vs. the real value of 47 ± 9 μJy, obtained by interpolating published JVLA flux densities to our observations) due to the low SNR. If we fix the source flux density to 47 ± 9 μJy, we get a size measurement of 1.3 ± 0.6 mas. As an additional test, we apply various Gaussian tapers to the uv-data to artificially lower our resolution, to see if we see missed extended flux in the source. While there is some small increase (up to 60 ± 12 μJy for a 0.5 taper at 20 Mλ) in the peak brightness, the SNR remains the same. A similar behaviour is seen for the AGN of NGC 4993. Therefore, the increase in peak brightness is just a combined effect of increasing noise in the tapered image, and some correlation losses at the longest baselines. Regardless the uv-taper, the peak brightness in our naturally weighted maps is fully consistent with the total flux density of 47 ± 9 μJy.

For these reasons, to be more quantitative, we implemented a Monte Carlo method to constrain the source size. We model the source as a circular Gaussian, with a given size and total flux. The flux is sampled from a normal distribution with mean 47 μJy and sigma 9 μJy (as interpolated to our epoch and frequency from the neighbouring JVLA data). We convolve the source with the measured synthetic beam of our untapered, naturally weighted, map. We add random realizations of the noise, taken directly from the real image (to account for noise non-gaussianity) to the resulting image. Then we record the source peak flux. Repeating the process many times for different sizes, we can then estimate the probability to get our measured peak flux (42 μJy) for a given size as the result of (1) noise fluctuations and (2) the source being partially resolved. Figure S3 shows the confidence level at which we can exclude source sizes larger than a given value. The blue dashed is obtained correcting for the 10% flux underestimate due to coherence losses at the largest baselines. By these results we conclude that the source size is smaller than 2 mas at the 90% confidence level.

Structured jet parameter estimation

We fit a power-law structured jet model (see Supplementary Text) to the 3 GHz, optical and X-ray light curves and to the centroid displacement as measured by comparing our position with those by the HSA (*22*). The model parameters are: core isotropic equivalent kinetic energy E_c, energy power law slope s_1, core Lorentz factor Γ_c, Lorentz factor slope s_2, core half-opening angle θ_c, Inter Stellar Medium (ISM) number density n, electron and magnetic field equipartition parameters ε_e and ε_B, post-shock electron power law index p and viewing angle θ_v. We fix p = 2.15 as indicated by the measured spectra, and we fix ε_e to its typical value 0.1. For the fit, we employ a standard Gaussian likelihood for all data points, with unequal sides in case of asymmetric error bars. In case of upper limits, we use a Gaussian penalty with a sigma equal to 10% of the value. The MCMC is performed using the emcee python package (*39*), employing 16 walkers, each running for 30000 steps. We assume uniform priors on $\log(E_c)$, s_1, $\log(\Gamma_c)$, s_2, θ_c, $\log(\varepsilon_B)$, $\log(n)$ and θ_v. We impose the bounds $\Gamma_c < 1000$, $\varepsilon_B > 10^{-5}$ and s_1, $s_2 < 8$ because of model degeneracy beyond these values. Once the MCMC is done, the best fit values are obtained by performing a principal component decomposition of the posterior samples, measuring the medians and then transforming back to the original base (the light curve of the jet with the resulting parameter values is shown with solid lines in Figure 3). The uncertainties are computed as the 16th and 84th percentiles of the posterior samples along each axis, thus representing one-sigma confidence ranges. The numerical values are reported in Table 1. We note that several

parameters show degeneracies, as it can be seen from the correlations in Figure S1. This means that there are several combinations of parameters compatible with the observed light curves and centroid displacement. The posterior distributions of Γ_c, s_2 and $\log(\varepsilon_B)$ do not show a peak, meaning that any value $\Gamma_c \geq 100$, $s_2 \leq 6$ and $\varepsilon_B \leq 0.03$ corresponds to a possible solution. Some other parameters, instead, are rather tightly constrained. Remarkably, the viewing angle is pinpointed to a rather low value $\theta_v \sim 15$ deg. It is worth pointing out, though, that our model does not account for the jet side expansion, which may affect slightly the observed flux centroid motion. We thus consider the uncertainty on this parameter possibly underestimated. Our analysis does not account for the information on the binary inclination that has been derived from the GW analysis. Assuming that the jet is launched in a direction perpendicular to the orbital plane, the binary inclination angle can be related to the jet viewing angle. The binary orbital plane inclination derived from the GW analysis, when the information on the host galaxy distance is included, is (*40*) $\iota = 151^{+15}_{-11}$ deg (90% confidence range). This range includes our best fit value 15 deg, even though it is near the edge of the range. Repeating the analysis using the GW results as a prior would yield a better (multi-messenger) estimate of this parameter: we plan to perform such an analysis in a future work.

Choked jet cocoon model parameters

We model the choked jet cocoon as described in Supplementary Text. We are unable to find a set of parameter values that fit the centroid displacement data (unless we assume an extremely narrow opening angle and a large energy, which thus falls back to the case of a jet), while we find that the light curves are well fitted by several parameter combinations. The size of radio image of the cocoon is mainly affected by the half-opening angle (i.e. by its degree of anisotropy), while the other parameters have only a minor impact. We thus choose a single set of parameters, and vary the half-opening angle, compensating the flux difference by changing the electron equipartition parameter ε_e correspondingly. All models thus have a viewing angle θ_v = 30 deg, a velocity profile $E(>\Gamma\beta) = E_0(\Gamma\beta)^{-\alpha}$ with $\alpha = 6$ and $E_0 = 1.5 \times 10^{52}$ erg, a maximum Lorentz factor $\Gamma_{max} = 6$ and a minimum ejecta velocity $\beta_{min} = 0.89$, an ISM number density $n = 1.8 \times 10^{-4}$ cm^{-3}, a post-shock magnetic field equipartition parameter $\varepsilon_B = 0.01$ and an electron power law slope $p = 2.15$ (these parameters are similar to those used by ref (*13*)). The values of the half-opening angle are θ_c = 30, 45 and 60 deg, and the corresponding electron equipartition parameter values are ε_e = 0.1, 0.05 and 0.045. The light curves are all the same, and correspond to the dashed lines in Figure 3.

Comparison of model images with Global VLBI source image

Since cleaning low-SNR data may result in unwanted artifacts in the image, and because our source appears unresolved, we just fitted a single 42 μJy point source component to the data to produce the naturally weighted and untapered map in DIFMAP. We applied an additional large scale, very shallow cleaning to smooth the noise around the source. The resulting image (shown in the upper left panel of Figure 1) was compared to simulated images for the successful jet and choked jet scenarios. To produce these latter images, we computed (see Supplementary Text) the predicted surface brightness distribution for the best fit successful jet model and for the three choked jet models described above. These images were read into AIPS, and then convolved with a beam of 3.5 × 1.5 mas with a 0 deg position angle using CONVL. We added noise with rms 8 μJy/beam (a noise map from the GRB 170817A field, but shifted in position, thus off the target) using COMB. The resulting images (shown in Figure 1 - note that the cocoons with θ_c =

45 and 60 deg are essentially identical, so only the former is reported) show that the successful jet reproduces the correct peak flux, while the cocoons are resolved and thus lead to a lower measured peak flux. Only the cocoon with θ_c = 30 deg can still be regarded as marginally consistent with the data, its peak flux being ~ 32 μJy/beam. However, the upper limit on the size as derived through the method described in the previous sections excludes this model which (Figure 2) should have a projectes size > 2 mas at our epoch.

Supplementary Text

Jet dynamics and parametrization of its angular structure

In order to compute the expected lightcurve and radio image of the jet, we need to know the dynamics of the jet expansion and deceleration into the interstellar medium (ISM). We assume, for simplicity, that the jet structure is axisymmetric, i.e. it depends only on the polar angle θ (i.e. on the angular distance from the jet axis) and not on the azimuthal angle φ. Let us call "jet element" a small portion of jet material comprised between θ and θ + dθ. As long as the jet element moves faster than the local sound speed, it is out of causal contact with the rest of the jet, and thus its dynamics in that phase must depend only on its initial bulk Lorentz factor $\Gamma_0(\theta)$, its kinetic energy per unit solid angle $dE(\theta)/d\Omega = dE(\theta)/2\pi \sin\theta d\theta$ and on the number density n of the ISM. Later on, as soon as the speed of sound waves close to the jet element becomes comparable to that of the expansion, the dynamics should start being affected by the surrounding jet elements, and thus should depend on the global jet structure, which makes it a much more difficult problem if analytical methods are to be employed. Nevertheless, numerical simulations indicate (*41*) that the energy transport in this phase is rather slow, so that the dynamics does not change drastically until at relatively late time. For these reasons, we neglect the effect of causal contact between neighbouring jet elements during the expansion, and we assume that each jet element expands and decelerates as if it were part of a spherical explosion with an isotropic equivalent kinetic energy $E_{K,iso}(\theta) = 4\pi\, dE(\theta)/d\Omega$ expanding adiabatically into the ISM. This assumption is common to most models of the structured jet dynamics used in the modelling of GRB 170817A so far (*11, 12, 42, 43*). Under these assumptions, the dynamics of each jet element can be computed by requiring conservation of energy as it sweeps the ISM (*44*). We parametrize the jet structure defining two functions:

$$E_{k,iso}(\theta) = \frac{E_c}{1 + (\theta/\theta_c)^{s_1}}$$

$$\Gamma(\theta) = 1 + \frac{\Gamma_c - 1}{1 + (\theta/\theta_c)^{s_2}}$$

which describe respectively the isotropic equivalent and initial Lorentz factor (i.e. the initial speed) as functions of the polar angle θ. This parametrization implies that these two quantities are constant within a jet core of half-opening angle θ_c and they decrease as power laws (of index s_1 and s_2, respectively) as a function of θ outside of it. The quantities θ_c, E_c, Γ_c, s_1 and s_2 are the parameters that define the structure.

Isotropic outflow dynamics and parametrization of its radial structure

The dynamics of the isotropic outflow expansion and deceleration are different from those of a jet element, because the outflow is assumed to have a radial velocity structure, i.e. the ejecta

in the outflow do not move all at the same velocity, but instead the kinetic energy is radially distributed between ejecta with a range of velocities. The outer, fastest ejecta shell first drives a shock in the ISM, which is then progressively reached by the inner, slower shells, which gradually contribute their energy to the shocked region. This effective, progressive energy injection results in a slower deceleration with respect to that of a shell with a single velocity. As soon as the slowest material has entered the shocked region, the deceleration turns back to follow the same laws as that of a uniform shell, because the energy injection from behind has stopped. The analytical solution for the dynamics can be derived again based on energy conservation (*45*).

The radial velocity profile can be specified by quantifying the amount of kinetic energy that is contained in the ejecta faster than each given velocity v, which we indicate as E(> v). This must be a decreasing function of v (by definition), and the faster it decreases, the smaller the fraction of energy contained in the fast tail of the ejecta. We employ the same parametrization as (*13*), namely

$$E(>v) = E_0 \times \begin{cases} 0 & v/c > \beta_{max} \\ \left(\dfrac{v/c}{\sqrt{1-v^2/c^2}}\right)^{-\alpha} & \beta_{min} < v/c < \beta_{max} \\ \left(\dfrac{v_{min}/c}{\sqrt{1-{v_{min}}^2/c^2}}\right)^{-\alpha} & v/c < \beta_{min} \end{cases}$$

which means that no significant energy is contained in ejecta faster than $\beta_{max}c$ or slower than $\beta_{min}c$, where c is the speed of light. The parameter α controls how steep is the decrease of the energy with velocity. We also introduce an additional parameter, namely the outflow half-opening angle θ_c. This allows us to account in a simple way for the possible anisotropy in the cocoon energy distribution.

We assume that both the jet and the isotropic outflow material emit synchrotron radiation and we neglect the contribution of Compton scattering of synchrotron or thermal photons, which is not expected to contribute significantly in the considered bands. Since the data do not seem to indicate any sign of synchrotron self-absorption in the source (*11*), we consider it to be optically thin, avoiding the computation of the effects of self-absorption for simplicity. In order to compute the image, we need to specify what is called the shock profile, i.e. how the energy and number density of electrons and magnetic field are distributed in the volume behind the shock. For the jet, in accordance with our assumptions on the dynamics, we assume that the shock profile at any fixed time, at any fixed polar angle is described by the Blandford-McKee self-similar spherical impulsive blastwave solution (*46*) with energy equal to the isotropic equivalent energy at that angle. For the spherical outflow, as long as the reverse shock is continuously crossed by the slower material, the shock profile does not resemble that of an impulsive explosion: the emission rather comes from a thin region comprised between the forward shock (which propagates into the ISM) and the reverse shock (which propagates back into the ejecta). As soon as the slowest ejecta have crossed the reverse shock, the profile turns back to that of an impulsive explosion. Since our observation took place after the peak of the light curve (i.e. after all the ejecta have crossed the reverse shock), we model the shock profile with the Blandford-McKee impulsive solution in this case as well.

Computation of the model images

Given all the assumptions described in the preceding sections, we compute the comoving synchrotron emissivity $j_{\nu'}$ on a 3D grid containing the emitting volume, at times (measured in the ISM frame) that correspond to the light cone of an observer on Earth who receives the photons at time t_{obs} = 207.4 d after GW170817, i.e. at the time of our global-VLBI observation. The emissivity is computed for emission at the comoving frequency corresponding to ν_{obs} = 5 GHz in the observer frame (taking into account both the Doppler shift and the cosmological redshift), and it is multiplied by the square of the Doppler factor to account for the relativistic transformation to the observer frame. Integration of the emissivities along the line of sight then results in a map of surface brightness, which is the source image.

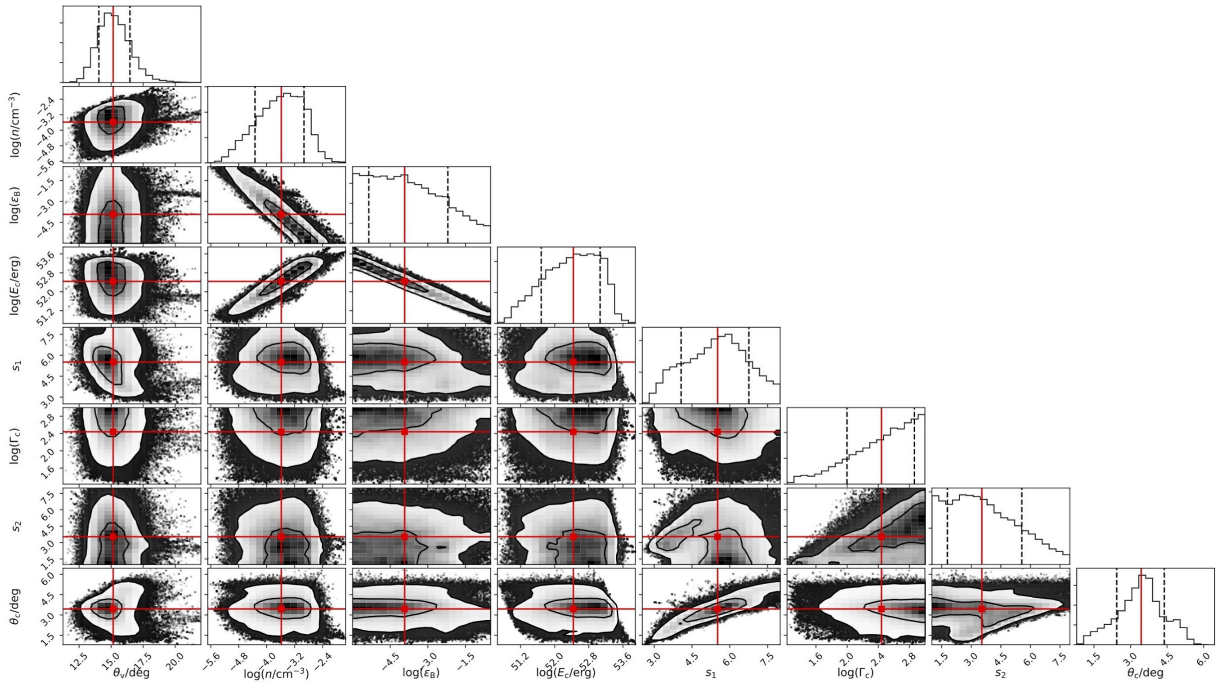

Fig. S1. Corner plot showing the results of our Markov Chain Monte Carlo parameter estimation for the structured jet model. The histograms on the diagonal show the marginalised posterior densities for each parameter. The remaining plots show the 2D joint posterior densi- ties of all couples of parameters, with 1σ and 2σ contours shown by black solid lines, and our best fit parameters shown by red squares and lines.

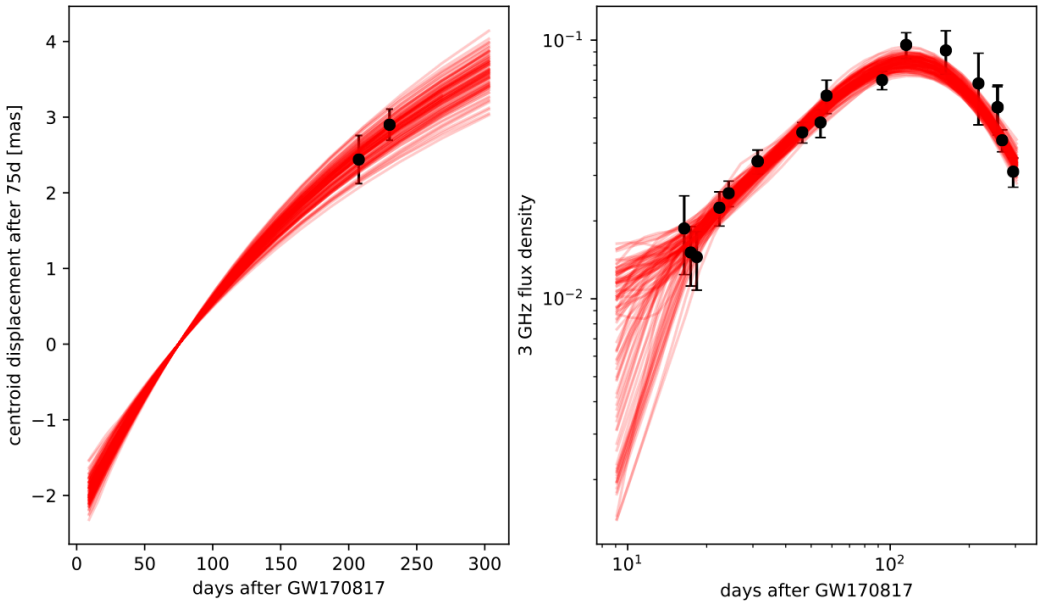

Fig. S2. Centroid displacement and 3 GHz light curve of 100 posterior samples from our Markov Chain Monte Carlo parameter estimation for the structured jet model. Left-hand panel: projected image centroid displacement in mas, as a function of the time since GW17817. The black points with error bars show the displacement measured comparing our position with those by the HSA. The red solid curves represent the centroid displacement with time corresponding to 100 randomly selected posterior samples. Right-hand panel: same as for the left-hand panel, but showing the 3 GHz radio light curve.

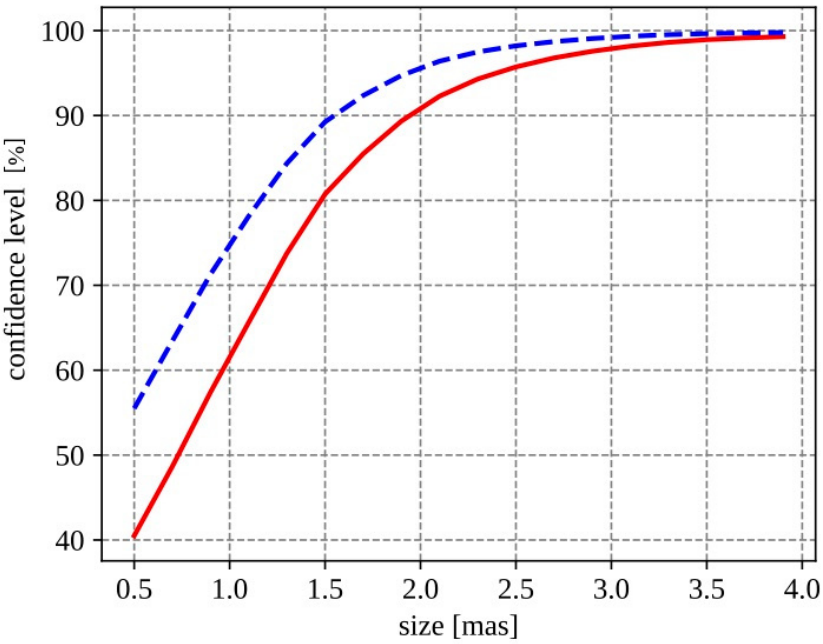

Fig. S3. Source size constraint. Confidence level of the source size to be smaller than a given size. This is obtained by convolving a Gaussian model for the source (with increasing size) with the measured image beam and adding it to the noise map. The curves show the probability probability to get our measured peak flux (42 μJy) for a given size as the result of (1) noise fluctuations and (2) the source being partially resolved. The dashed blue line accounts also for the possible 10% loss in the flux measurement due to coherence losses on the longest baselines.

Parameter	best fit value	one sigma range
	Flat prior on $\theta_{\rm v}$	
$\log(E_{\rm c}/{\rm erg})$	52.4	$(51.7, 53.0)$
s_1	5.5	$(4.1, 6.8)$
$\log(\Gamma_{\rm c})$	2.4	$(2.0, 2.9)$
s_2	3.5	$(1.8, 5.6)$
$\theta_{\rm c}/{\rm deg}$	3.4	$(2.4, 4.4)$
$\log(\epsilon_{\rm B})$	-3.9	$(-5.4, -2.2)$
$\log(n/{\rm cm}^{-3})$	-3.6	$(-4.3, -2.9)$
$\theta_{\rm v}/{\rm deg}$	15	$(14, 16.5)$

Table S1. Results of our parameter estimation for the structured jet model.